

## 1. Introduction

M82 is among the most extensively studied galaxies, with decades of high resolution observations having been facilitated by the M81 group’s close proximity ( $D \simeq 3.63$  Mpc; Karachentsev et al. 2004). M82 is considered the “prototypical” starbursting galaxy, featuring a bipolar superwind outflow that extends kiloparsecs along the minor axis of the galaxy. Many of M82’s features, including a disturbed disk and the starburst itself, are thought to have been triggered by the recent passage of M81  $\sim 200$ – $300$  Myr ago (e.g., Cottrell 1977). Studies of the neutral and molecular hydrogen in M82 have found evidence of tidally induced structures, including disruption of the gas from the disk of M82 (e.g., Sofue 1998) and a significant amount of gas located in the field and in tidal bridges between M81, M82, and NGC 3077 (e.g., Yun et al. 1994).

This environment makes the M81 group conducive to the formation of tidal dwarf galaxies (TDGs), which form in the tidal arms and bridges induced by galaxy encounters. Gravitational instabilities develop in the absence of the rotational support that existed in the disk, and the Jeans mass rises due to the additional dispersion created by the heating of the material during the encounter (e.g., Duc et al. 2000; Struck et al. 2005). In contrast to typical low-mass dwarf galaxies, TDGs have little to no dark matter and have metallicities commensurate with their progenitor spirals rather than the range expected from the dwarf mass–metallicity relation (e.g., Duc et al. 2004; Bournaud & Duc 2006).

The creation rate of TDGs and their survivability rates are poorly constrained, but have potential impacts on the interpretation of satellite population statistics in a  $\Lambda$ CDM framework.

Several of the dwarf galaxies in the M81 group are thought to be TDGs, including Holmberg IX, BK3N, Arp-loop (A0952+69), and Garland (e.g., Makarova et al. 2002; Weisz et al. 2008; de Mello et al. 2008; Sabbi et al. 2008); however, none of these candidate TDGs or TDG progenitors are located in the vicinity of M82, instead clustering near M81 and NGC 3077. Indeed, no regions of active star formation have been reported in and around M82 outside the galactic disk.

We have used a novel telescope built on the framework of the Dragonfly Telephoto Array (Abraham & van Dokkum 2014), the 3 lens narrowband *pathfinder* version of the forthcoming Dragonfly Spectral Line Mapper (*p*DLSM), to image low-surface-brightness emission in the M81 group in  $H\alpha$  and [N II]. We selected the M81 group to vet the narrowband design because deep prior  $H\alpha$  observations exist, providing a test of the depths being reached by the instrument. Our final  $H\alpha$  images of the field reach surface brightness depths of  $\sim 5 \times 10^{-19}$  erg s $^{-1}$  cm $^{-2}$  arcsec $^{-2}$  and uncover several new features in the gas around M82 that will be described in forthcoming work. Details of the *p*DLSM instrument are provided in Lokhorst et al. (2019, 2020).

In this Letter, we present the analysis of an  $H\alpha$  object near M82 that is likely a TDG in formation, using the first science data obtained with this instrument. We have designated this source DF–E1 (“Sapling”), as it is the first emission source cataloged by Dragonfly.

## 2. Narrowband Imaging

### 2.1. Observations

The *p*DLSM builds on the telephoto array concept of Dragonfly by placing ultra-narrowband interference filters

---

<sup>8</sup> NSF Graduate Research Fellow.



Original content from this work may be used under the terms of the [Creative Commons Attribution 4.0 licence](https://creativecommons.org/licenses/by/4.0/). Any further distribution of this work must maintain attribution to the author(s) and the title of the work, journal citation and DOI.

( $\Delta\lambda = 0.8 - 3$  nm) in front of each lens of the array, targeting H $\alpha$  and [N II] via tilting of the filters, and [O III].

The M81 group was observed with the *p*DLSM over the course of several weeks during the spring of 2020 at both H $\alpha$  and [N II] tilts. Observations were carried out semi-autonomously, with a dither pattern of 15' between exposures. Individual frames had exposure times of 1800 s. During data reduction, low-quality frames were automatically identified and removed. Frames ultimately used in this analysis were also checked by eye to ensure quality; some frames were removed due to light contamination from sources in the dome or were cropped due to significant amplifier glow in corners of the frame.

The final images presented here comprise 190 frames in H $\alpha$  (taken across the three lenses in the pathfinder array), for a “single-lens” total exposure time of 95 hr, and 89 frames in [N II] for an total exposure time of 44.5 hr. Individual images were flatfielded and dark-current subtracted using calibration frames taken nearest each observation temporally.

## 2.2. Continuum Subtraction and Flux Calibration

Continuum subtraction was performed using exposures taken with the Dragonfly Telephoto Array in the Sloan-*r* band. These images have similar pixel scales and point-spread functions to the images taken with the *p*DLSM setup. An effective scaling factor of 11.3 was determined between the continuum image and the narrowband images, using a combination of aperture photometry on stars in the field as well as apertures placed on the disk of M82. We used the *SourceExtractor* package (Bertin & Arnouts 1996) to identify and mask any point-like sources in images prior to continuum subtraction.

Published fluxes of H II regions in M81 were used to directly calibrate our image counts; while not shown in the cutouts presented here, M81 was in the imaging field of view. We selected two independent data sets to use, one from Lin et al. (2003), the other from Patterson et al. (2012), which present spectrally calibrated H $\alpha$ + [N II] fluxes and H $\alpha$  luminosities, respectively. We defined one calibration by combining our [N II] and H $\alpha$  images and comparing to Lin et al. (2003) and another by comparing to the fluxes implied by the Patterson et al. (2012) luminosities to our H $\alpha$  image alone.

For each calibration, we computed best-fit relations in log space using a first-degree polynomial in an iterative sigma-clipping routine that eliminates outliers of  $>3\sigma$  in each iteration. Both calibrations were consistent with each other, with no observed systematic offset. Due to the greater number of H II regions included and marginally tighter scatter, we have adopted the best-fit relation to the Lin et al. (2003) observations in this work, which has a derived calibration of

$$\log(F) [\text{erg s}^{-1} \text{cm}^{-2}] = 0.99 \log(\text{cts}) - 16.801, \quad (1)$$

where log is base 10 (adopted throughout). Based on the scatter in the fit relation, we estimate the calibration uncertainty is  $\sim 5\%$  in flux. Additional details regarding the instrument, reduction, and calibration are provided in a companion paper (D. L. Lokhorst et al. 2021, submitted).

## 3. An H $\alpha$ Object near M82

A summary of measurements presented in the following sections is provided in Table 1.

**Table 1**  
Properties of DF-E1

Source Property	Value
R.A.	09 56 32.184
decl.	+69 42 45.453
$v_{\text{helio}}$	276.7 ( $\pm 25$ ) km s $^{-1}$
$v_{\text{helio}} - v_{\text{M82}}$	73.7 ( $\pm 25$ ) km s $^{-1}$
Diameter <sup>a</sup> (arcsec)	34.6''
Diameter <sup>b</sup> (pc)	608 pc
H $\alpha$ Flux <sup>c</sup>	$(6.5 \pm 0.9) \times 10^{-14}$ erg s $^{-1}$ cm $^{-2}$
[N II] Flux <sup>c</sup>	$(2.9 \pm 0.4) \times 10^{-14}$ erg s $^{-1}$ cm $^{-2}$
[N II]/H $\alpha$ ( <i>p</i> DLSM)	0.38 $\pm$ 0.06
[N II]/H $\alpha$ (LRIS)	0.31 $\pm$ 0.015
[O III]/H $\beta$ (LRIS)	0.34 $\pm$ 0.07
12+log(O/H) (via <i>O3N2</i> )	8.67 $\pm$ 0.14
L(H $\alpha$ ) <sup>c</sup>	$(1.03 \pm 0.14) \times 10^{38}$ erg s $^{-1}$
log SFR(H $\alpha$ )	-2.39 $\pm$ 0.03
FUV Flux Density	$(2.73 \pm 1.1) \times 10^{-14}$ erg s $^{-1}$ cm $^{-2}$ $\text{\AA}^{-1}$
log SFR(FUV) <sup>c</sup>	-2.317
H I Mass	$\sim 5 \times 10^7 M_{\odot}$

### Notes.

<sup>a</sup> Defined as the mean FWHM of a Gaussian fit to the Dragonfly image.

<sup>b</sup> Assuming a distance of 3.63 Mpc.

<sup>c</sup> Not corrected for dust attenuation.

## 3.1. The H $\alpha$ Feature Seen with the *p*DLSM

An H $\alpha$  image from *p*DLSM of M82 is presented in Figure 1. DF-E1 is  $\sim 4.3$  kpc from the galactic center and 493 pc above the midplane ( $\sim 3 h_z$ ; Lim et al. 2013). While several H $\alpha$  maps from previous studies (e.g., Lehnert et al. 1999; Hoopes et al. 2005; Karachentsev & Kaisin 2007) show evidence for H $\alpha$  emission overdensities at DF-E1’s location, the detections were not discussed in those works. To our knowledge, no study has specifically referenced this H $\alpha$  object.

DF-E1 has a well-defined peak in the Dragonfly data and exhibits lobes of elongation in both the north-south and east-west directions, resembling an “L-shaped” blob. We measure the size of DF-E1 from the *p*DLSM imaging by fitting Gaussians to the flux profile of the source along both the north-south and east-west position angles, passing through the peak flux location. The average of the two fits was kept. The two fits were nearly identical, with a full width half maximum (FWHM) value of 34.''6 and 95% width of 58.''8, corresponding to linear scales of 608 pc and 1034 pc, respectively.

The flux of the source in the aperture defined by the FWHM is  $\sim 6.5 \times 10^{-14}$  erg s $^{-1}$  cm $^{-2}$ . We did not explicitly correct for a background contribution to the flux from M82, but note that in the region around but not including the source, the H $\alpha$  background is  $\sim 10\%$  of the measured flux, which we adopt into our uncertainty. We measured the [N II] flux similarly, obtaining  $F_{[\text{NII}]} = 2.9 \times 10^{-14}$  erg s $^{-1}$  cm $^{-2}$ , corresponding to an [N II]/H $\alpha$  ratio of  $0.38 \pm 0.06$ , in line with typical values for star-forming regions, and in general lower than the disk of M82, which is known to have elevated [N II]/H $\alpha$  ratios due to turbulence and shocks (e.g., Shopbell & Bland-Hawthorn 1998).

The corresponding dust-uncorrected H $\alpha$  luminosity of the source is  $1.03 \times 10^{38}$  erg s $^{-1}$ . To estimate a star formation rate from this value, we used the calibration from Lee et al. (2009):

$$\log \text{SFR} [M_{\odot} \text{yr}^{-1}] = 0.62 \log(7.9 \times 10^{42} L_{\text{H}\alpha}) - 0.47, \quad (2)$$

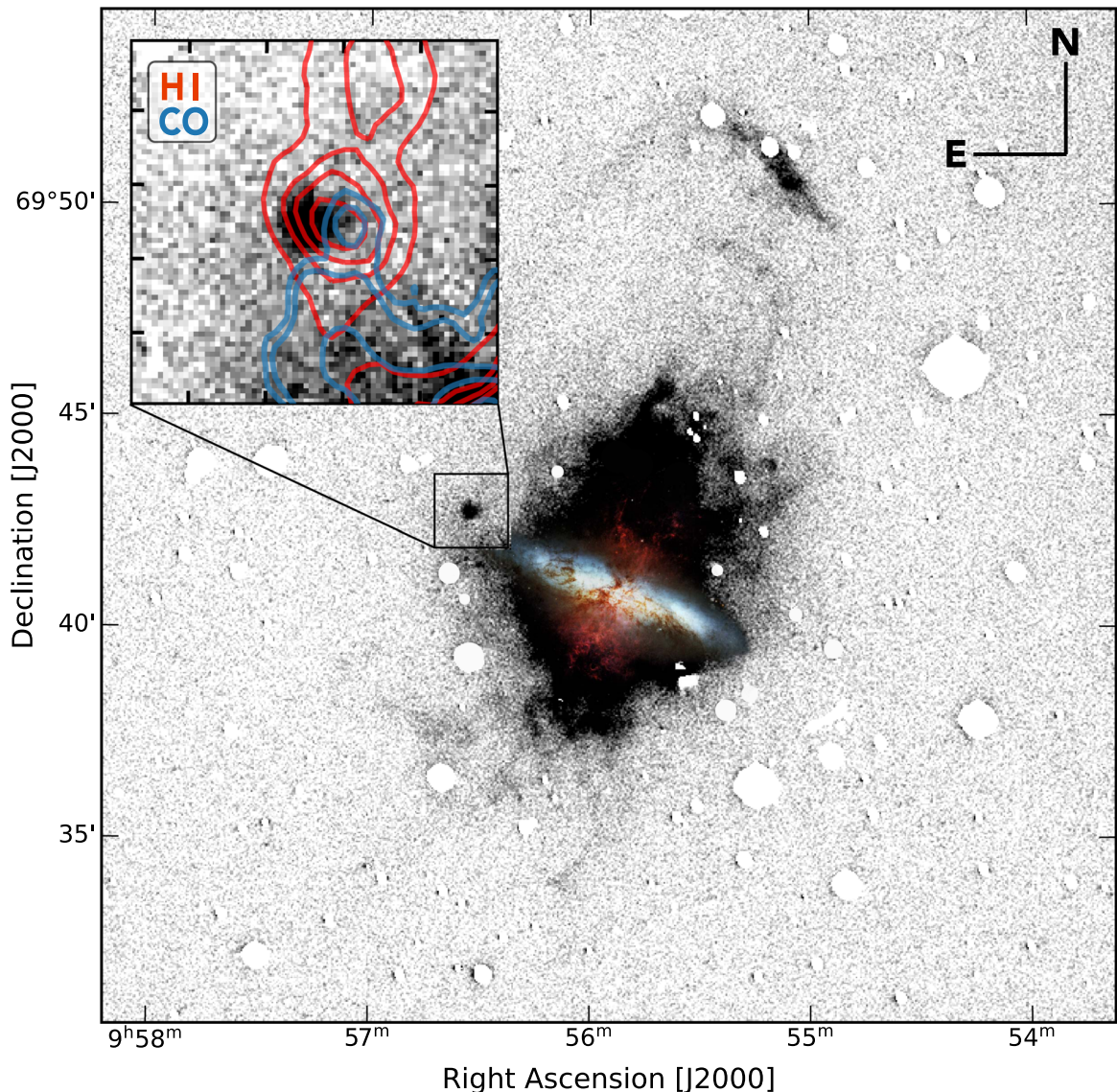


**Figure 1.** *p*DLSM continuum-subtracted image of M82 in  $H\alpha$ , with foreground stars masked. The HST composite image of M82 from Mutchler et al. (2007) has been overlaid for a sense of scale. An inset panel shows a  $2.5 \times 2.5$  square cutout around DF-E1, with red contours showing H I from de Blok et al. (2018, dB18 hereafter) and blue contours showing CO from Leroy et al. (2015, L15 hereafter) in the region overlaid. The strongest overdensity of the northern H I tidal arm spatially overlaps with DF-E1, with the peak of the H I emission falling within  $15''$  of the peak of the  $H\alpha$  source. Similarly, an overdensity of CO is present, consistent with the H I peak.

where  $L_{H\alpha}$  is in  $\text{erg s}^{-1}$ . We selected this calibration as it is (a) tuned to local dwarf galaxies with  $H\alpha$  luminosities in the range of  $10^{37}$  to  $2.5 \times 10^{39}$   $\text{erg s}^{-1}$ , matching our source and (b) is calibrated using the extinction-corrected FUV- $H\alpha$  relation to be intrinsically dust-correcting. Using this calibration, we obtained an SFR of  $0.004 M_{\odot} \text{ yr}^{-1}$  ( $\log \text{SFR} = -2.39$ ).

### 3.2. Far-UV and Optical Imaging

If DF-E1 is indeed forming stars, then we expect cospatial FUV emission. In Figure 2 we present Galaxy Evolution Explorer (GALEX) imaging from Hoopes et al. (2005) of M82, as well as F435W, F814W, and F658N imaging from HST (Mutchler et al. 2007). We identify several regions of concentrated FUV emission within the extent of DF-E1, indicating the existence of young O/B stars. That this emission is not a background source is confirmed by the F435W imaging, which resolves the FUV clumps into several regions containing one or more bright point sources and at least one

clustering of stars, which we note are found to form efficiently in TDGs (Fensch et al. 2019). These sources furthermore align with the ionized gas in the region.

Because TDGs form in tidal arms where dust content is expected to be minimal compared to the host galaxy, FUV emission provides a useful direct probe of ongoing star formation. Leveraging this expected consistency, we use the  $H\alpha$ -derived SFR to infer the expected ionizing FUV flux and compare this with the GALEX data. We convert the  $H\alpha$ -derived SFR via Kennicutt (1998):

$$\text{SFR} [M_{\odot} \text{ yr}^{-1}] = 1.4 \times 10^{-28} L_{\text{FUV}} [\text{erg s}^{-1} \text{ Hz}^{-1}], \quad (3)$$

which predicts a FUV flux of  $1.83 \times 10^{-26}$   $\text{erg s}^{-1} \text{ cm}^{-2} \text{ Hz}^{-1}$ . We measure the FUV flux directly in an  $11''$  aperture, as the emission is more concentrated than the  $H\alpha$ . Given the extremely low UV background in GALEX FUV, we assume Poisson uncertainties on the counts. This produces an FUV flux of  $(2.2 \pm 0.5) \times 10^{-26}$   $\text{erg s}^{-1} \text{ cm}^{-2} \text{ Hz}^{-1}$ , consistent with the

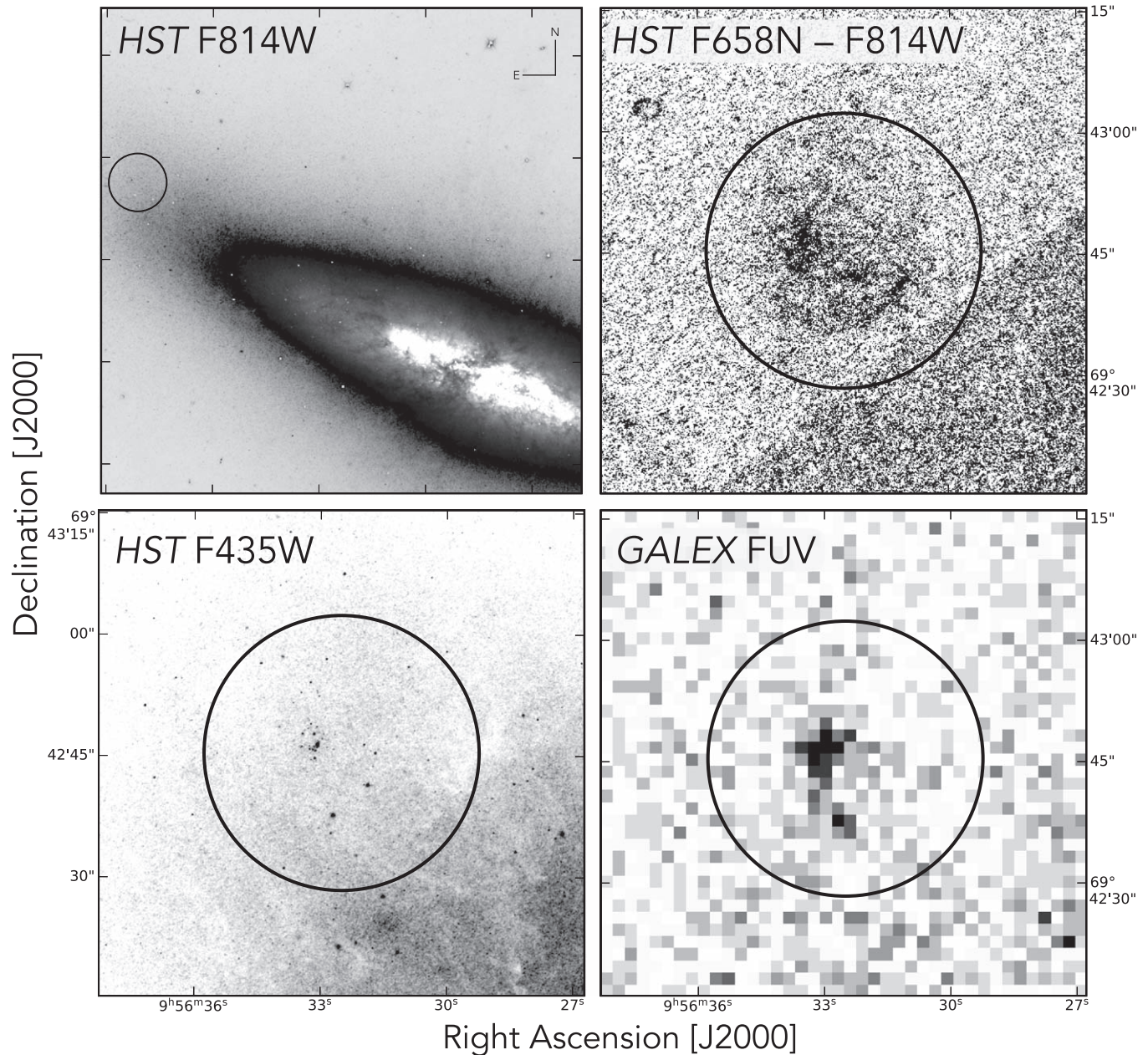


**Figure 2.** DF–E1 in HST F814W (top left), continuum-subtracted F658N (top right), F435W (bottom left), and GALEX FUV (bottom right). The F814W panel serves to contextualize DF–E1’s position and size with respect to M82; note the inner part of M82 is shown in an inverse color scaling for visual clarity. The other three panels demonstrate a strong correspondence between the  $H\alpha$  emission morphology of DF–E1, resolved point sources in HST F435W, and FUV emission.

predicted FUV value. In the absence of resolved HST imaging, it is clear from Figure 2 that UV emission is a valuable locator of the star-forming sites *within* the diffuse  $H\alpha$  emission region or H I extent of these objects (e.g., Mundell et al. 2004; Neff et al. 2005).

### 3.3. Neutral and Molecular Hydrogen

DF–E1 is spatially coincident with the base of a several kpc-long structure known as the “countertail,” or Northern H I streamer (Yun et al. 1993, hereafter Y93). This feature is theorized to have been torqued northward—opposite another H I stream in the southwest which extends down toward M81—after the close passage of the two galaxies several hundred Myr ago.

The overdensity of H I in the stream at the location of DF–E1 can be seen in Figures 1 and 3 (left). The H I gas mass for the full countertail, calculated via

$$M_{\text{HI}} = 2.356 \times 10^5 D^2 \int S_\nu dv \quad (4)$$

where  $S_\nu$  is in Jy and  $D$  is in Mpc, is  $\sim 2 \times 10^8 M_\odot$ , with  $\sim 5.1 \times 10^7 M_\odot$  in an aperture cospatial with the  $H\alpha$  source in the moment 0 map. For mass calculations we use the available zero-spacing corrected data cube from dB18 which combines the sensitivity of previous single dish observations (Chynoweth et al. 2008) with the high resolution data gathered by dB18. The H I gas in this region has a mean velocity of  $45 \text{ km s}^{-1}$  with respect to M82’s recession velocity, with a  $1\sigma$  spread of  $47 \text{ km s}^{-1}$  along the

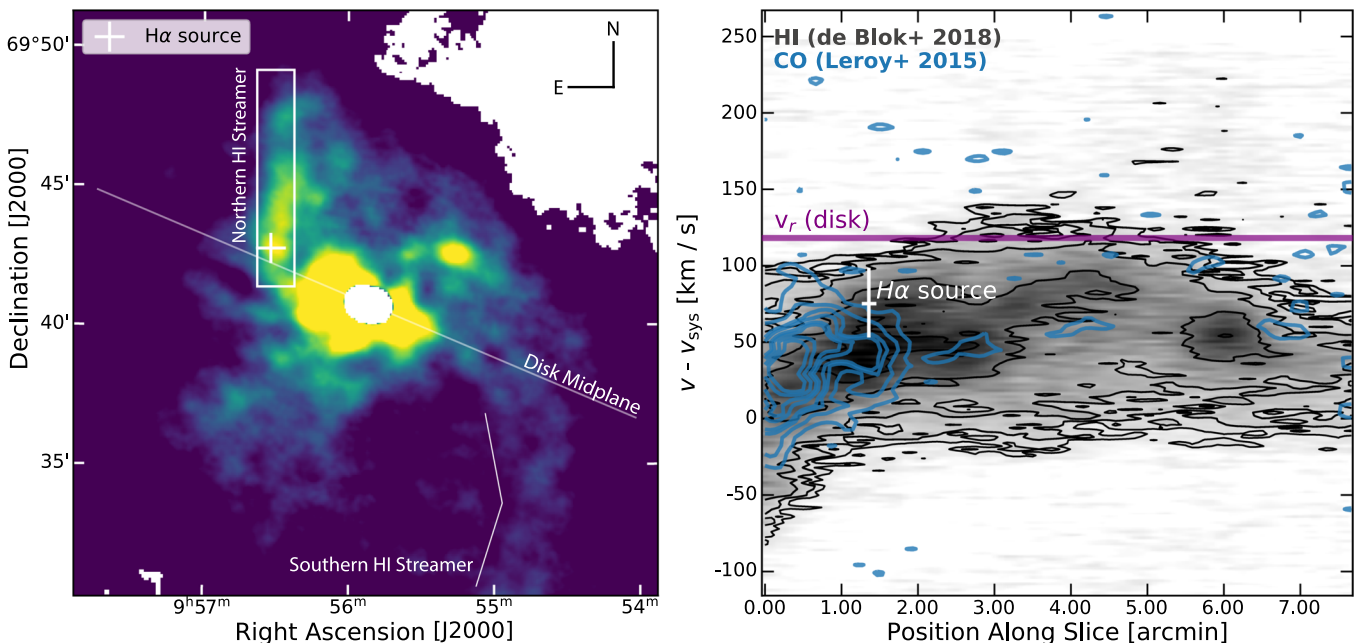


**Figure 3.** H I Moment 0 map from dB18 (left), with tidal features and the disk midplane labeled. In the right panel, we extract a position–velocity diagram along the slice indicated by the white aperture in the left panel from both the H I and CO data. The location of DF–E1 in position–velocity space is indicated by a plus, demonstrating its velocity correspondence with the tidal feature.

line of sight (Figure 3, right). It is well known that this gas is kinematically decoupled from the disk of M82 (e.g., Sofue 1998), as the disk has a rotation velocity of  $\sim 120 \text{ km s}^{-1}$  at roughly the position of DF–E1 (Greco et al. 2012).

Given the presence of star formation, we would also expect to see kinematically and spatially coincident molecular hydrogen in the general vicinity of DF–E1. Indeed, CO ( $J = 2 \rightarrow 1$ ) data from L15 show an overdensity in the  $251 \text{ km s}^{-1}$  channel. This corresponds to a velocity of  $42 \text{ km s}^{-1}$  with respect to M82’s recession—in strong agreement with the peak of H I emission (Figure 3).

While the spatial alignment of H $\alpha$  and FUV emission of DF–E1 with that of H I and CO strongly suggests a star-forming object within the tidal streamer, unambiguously confirming the association of the H $\alpha$  region and ionizing sources with the tidal feature rather than the disk of M82 requires detailed velocity information for DF–E1. To this end, we obtained optical spectroscopy with Keck.

#### 4. Keck/LRIS Spectroscopy

Red-side and blue-side spectroscopy of DF–E1 was carried out using the LRIS spectrograph (Oke et al. 1995; Rockosi et al. 2010) mounted on the Keck I telescope on the nights of 2021 April 14 and 2021 May 07, respectively. While the primary goal was to obtain the velocity of the source, we also obtained relevant diagnostic line ratios, including  $[\text{N II}]/\text{H}\alpha$  and  $[\text{O III}]/\text{H}\beta$ .

Conditions during the runs were clear and the seeing was stable at  $\sim 0''.6$  and  $\sim 1''.3$  for the two nights, respectively. Exposures were obtained using the  $1''.5$  wide,  $168''$  long slit, using the 560 nm dichroic, 600/4000 grism, and 1200/7500 grating with a  $39^\circ$  dispersion angle to place  $6563 \text{ \AA}$  at the center of the red-side detector. M82 was observed at its highest elevation, which corresponded to an air mass of  $\sim 1.5$ . Two

consecutive 600 s exposures were obtained. The long slit was aligned with the brightest knot of emission determined from the HST data with a position angle of  $-15^\circ$ .

Reduction was carried out using the PyPeIt pipeline (Prochaska et al. 2020) using the settings for `lris_red` and `lris_blue`. Instrumental flats and arcs obtained at the beginning of the evening—as well as skylines in the science exposures—were used to trace the slit edges and perform wavelength calibration, sky modeling, and sky subtraction.

Extracted 1D spectra (observed frame) are presented in Figure 4, with relevant emission lines denoted. Wavelengths are shown in vacuum, and a heliocentric correction of  $-18 \text{ km s}^{-1}$  was applied during reduction. Due to a skyline near H $\alpha$  which was not fully removed in the PyPeIt reduction, we re-reduced the frames using sky backgrounds to measure the H $\alpha$  flux.

To determine the velocity of DF–E1, we fit a model to the four other emission lines in the red using `emcee` (Foreman-Mackey et al. 2013). Emission lines were fit with Gaussians, with amplitudes and widths left free. We constrained the wavelength differences between the lines to their intrinsic separations, and fit for a single wavelength shift.

We find a best-fit velocity of  $276.7 \text{ km s}^{-1}$ , with a  $1\sigma$  posterior spread of  $1.12 \text{ km s}^{-1}$ ; the velocity uncertainty is dominated by the calibration uncertainty, which we estimate to be  $25 \text{ km s}^{-1}$ . Assuming a heliocentric-corrected velocity for M82 of  $203 \text{ km s}^{-1}$  (de Vaucouleurs et al. 1991), this corresponds to a velocity of  $73.7 \text{ km s}^{-1}$  with respect to the recession velocity of M82, indicating conclusively that DF–E1 is not embedded within the rotating disk ( $\sim 120 \text{ km s}^{-1}$ ). This is shown in Figure 3 (right), in which DF–E1’s velocity is well within the envelope of the H I gas and well separated from the rotation velocity of M82.

We also extract line ratios from our spectroscopy, finding  $[\text{N II}]/\text{H}\alpha = 0.31 \pm 0.015$  and  $[\text{O III}]/\text{H}\beta = 0.34 \pm 0.07$ . Using

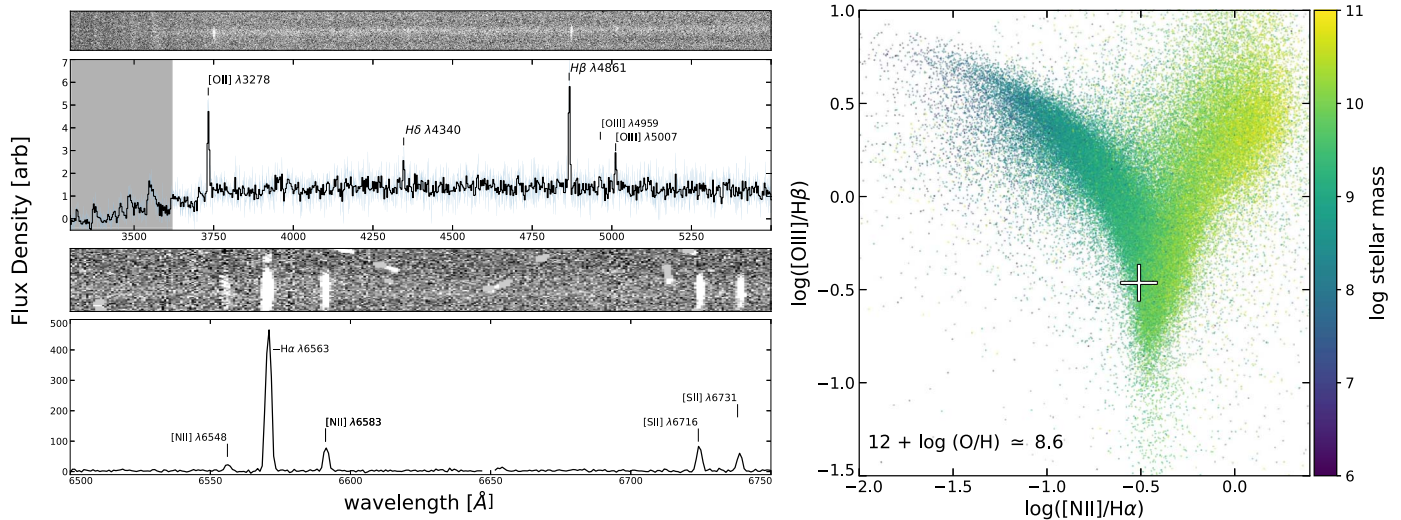


**Figure 4.** Left: extracted LRIS spectrum of DF–E1 in the blue (top) and red side (bottom). On the blue side, we show the raw spectrum in blue and one binned by 3 pixels in black. We readily detect  $H\alpha$ , both [N II] lines, both [S II] lines,  $H\beta$ , [O II], [O III] (5007 Å and 4959 Å), and  $H\delta$ . The source’s velocity is estimated by performing a Bayesian fit to four lines on the red side. Right: BPT diagram showing DF–E1’s location (white plus) relative to SDSS galaxies from the NASA Sloan Atlas, colored by stellar mass.

the O3N2 metallicity calibration of Pettini & Pagel (2004),

$$12 + \log(\text{O}/\text{H}) = 8.73 - 0.32 \times \text{O3N2}, \quad (5)$$

we find that DF–E1 has a metallicity of  $8.67 \pm 0.14$ , similar to metallicities found in other TDGs (e.g., Lisenfeld et al. 2008) and consistent with the star-forming gas being pre-enriched—as one would expect for gas liberated from the galactic disk of a massive spiral galaxy (e.g., Duc et al. 2000; Recchi et al. 2015). This is reflected in Figure 4 (right), where on the Baldwin, Phillips, and Telervich (BPT) diagram, DF–E1 falls on the locus of star-forming galaxies, here drawn from the NASA Sloan Atlas (Blanton et al. 2011), in a location consistent with M82’s log stellar mass of  $\sim 9$ – $9.5$ .

## 5. Discussion

Based on these observations, DF–E1 is an object similar to other claimed tidal dwarf galaxies that have been recently discussed in the literature (e.g., Mundell et al. 2004; Querejeta et al. 2021; Román et al. 2021). If it survives the eventual dissipation of the tidal streamer and does not fall back into M82, it will join the ranks of dwarf satellite galaxies in the M81 group.

Many objects of this type, however, are transient in nature, quickly falling back into the galactic disk (Bournaud & Duc 2006). The tidal tail that houses this complex of star-forming regions is only several hundred Myr old and numerical simulations suggest that a  $\sim$ Gyr of decoupled evolution is needed before one can unambiguously declare an object a TDG. DF–E1 has properties that both aid and hinder its potential longevity. The velocity of the tidal arm and DF–E1 is prograde with respect to M82’s rotation, which has been found to be helpful in maintaining the TDG over time (Bournaud & Duc 2006). Conversely, the most successful TDGs seem to be those that form at the very tip of tidal arm structures (as far as possible from their original host). DF–E1 is near the base of the tidal structure. An important factor governing its survival is the velocity at which the arm (and TDG progenitor within) is

moving upward and away from M82; however, this motion is primarily in the sky plane and is thus unconstrained.

Further complicating this picture is the broader environment of M82. Over the next Gyr, simulations indicate that the main galaxies in the group, M81, M82, and NGC 3077, are likely to merge (Yun 1999; Oehm et al. 2017), making the fate of this particular object an open question. It is interesting to consider whether any other TDGs may be forming in this region; if there are, they would likely be found farther up along the northern tidal streamer or along the southern streamer toward M81. Deeper, higher S/N observations with the upgraded *p*DLSM will be needed to investigate this possibility.

Ultimately, DF–E1 is a strong candidate for a young TDG, is in the earliest stages of its formation, and is remarkably nearby, at  $\sim 3.6$  Mpc, making it a prime candidate for resolved studies of the earliest stages of this class of object.

We thank the anonymous referee whose comments and suggestions improved the quality of this work. We thank Todd Thompson and Natascha Förster Schreiber for valuable discussion and feedback. I.P. is supported by the National Science Foundation Graduate Research Fellowship Program under grant No. DGE1752134. Some of the data presented herein were obtained at the W. M. Keck Observatory, which is operated as a scientific partnership among the California Institute of Technology, the University of California, and the National Aeronautics and Space Administration. The Observatory was made possible by the generous financial support of the W. M. Keck Foundation. The authors wish to recognize and acknowledge the very significant cultural role and reverence that the summit of Maunakea has always had within the indigenous Hawaiian community. We are most fortunate to have the opportunity to conduct observations from this mountain. This research is based on observations made with the NASA/ESA Hubble Space Telescope obtained from the Space Telescope Science Institute, which is operated by the Association of Universities for Research in Astronomy, Inc., under NASA contract NAS 526555. These observations are associated with program 10776 (PI: Matt Mountain). The authors thank the staff at New Mexico Skies Observatory for their support and aid in maintaining the

*p*DSLIM instrument. The Dunlap Institute is funded through an endowment established by the David Dunlap family and the University of Toronto.

*Facility:* Keck:I (LRIS); Dragonfly Telephoto Array.

*Software:* `numpy` (Van Der Walt et al. 2011), `astropy` (Astropy Collaboration et al. 2018), `matplotlib` (Hunter 2007), `emcee` (Foreman-Mackey et al. 2013), `PyPeIt` (Prochaska et al. 2020), `SExtractor` (Bertin & Arnouts 1996).

Foreman-Mackey, D., Hogg, D. W., Lang, D., & Goodman, J. 2013, *PASP*, **125**, 306

Greco, J. P., Martini, P., & Thompson, T. A. 2012, *ApJ*, **757**, 24

Hoopes, C. G., Heckman, T. M., Strickland, D. K., et al. 2005, *ApJL*, **619**, L99

Hunter, J. D. 2007, *CSE*, **9**, 90

Karachentsev, I. D., & Kaisin, S. S. 2007, *AJ*, **133**, 1883

Karachentsev, I. D., Karachentseva, V. E., Huchtmeier, W. K., & Makarov, D. I. 2004, *AJ*, **127**, 2031

Kennicutt, R. C. J. 1998, *ARA&A*, **36**, 189

Lee, J. C., Gil de Paz, A., Tremonti, C., et al. 2009, *ApJ*, **706**, 599